Solder–Graphite Network Composite Sheets as High-Performance Thermal Interface Materials

Munish Sharma & D. D. L. Chung

Journal of Electronic Materials

ISSN 0361-5235
Volume 44
Number 3

Journal of Elec Materi (2015) 44:929-947
DOI 10.1007/s11664-014-3589-0

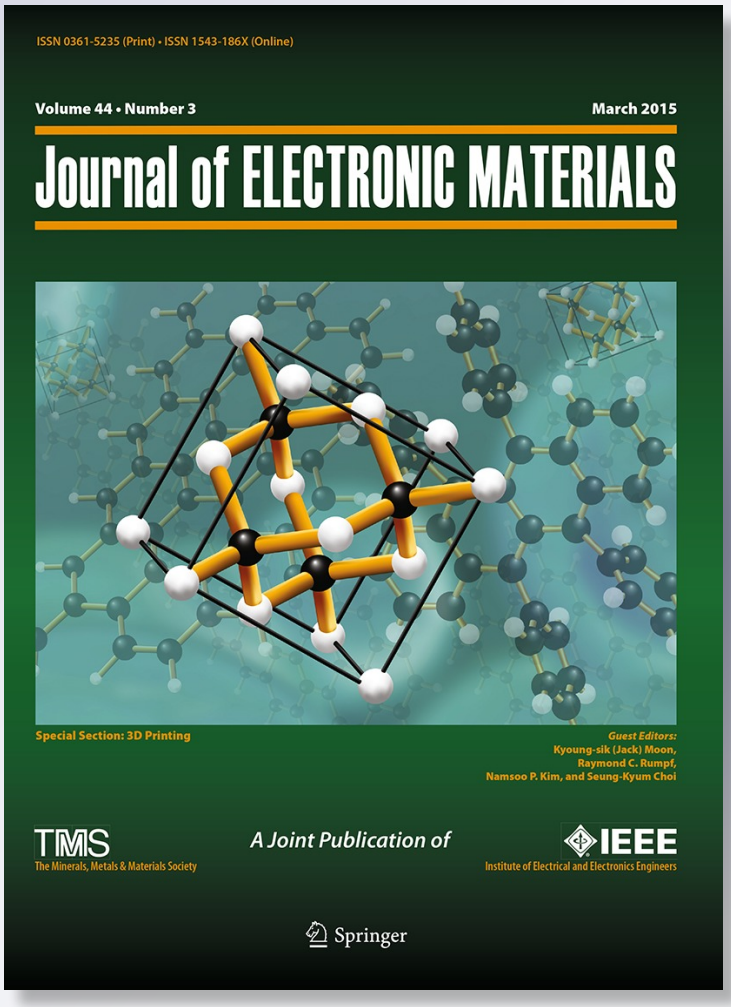

Springer

Journal of ELECTRONIC MATERIALS, Vol. 44, No. 3, 2015
DOI: 10.1007/s11664-014-3589-0

Solder–Graphite Network Composite Sheets as High-Performance Thermal Interface Materials

MUNISH SHARMA[1] and D.D.L. CHUNG[1,2]

1.—Composite Materials Research Laboratory, University at Buffalo, State University of New York, Buffalo, NY 14260-4400, USA. 2.—e-mail: ddlchung@buffalo.edu

Low-cost solder–graphite composite sheets (≥55 vol.% solder), with solder and graphite forming interpenetrating networks to a degree, are excellent thermal interface materials (TIMs). Solders 63Sn-37Pb and 95.5Sn-4Ag-0.5Cu are separately used, with the latter performing better. In composite fabrication, a mixture of micrometer-size solder powder and ozone-treated exfoliated graphite is compressed to form a graphite network, followed by fluxless solder reflow and subsequent hot pressing to form the solder network. The network connectivity (enhanced by ozone treatment) is lower in the through-thickness direction. The electrical conductivity obeys the rule of mixtures (parallel model in-plane and series model through-thickness), with anisotropy 7. Thermal contact conductance $\leq 26 \times 10^4$ W/(m^2 K) (with 15-μm-roughness copper sandwiching surfaces), through-thickness thermal conductivity ≤52 W/(m K), and in-plane thermal expansion coefficient 1×10^{-5}/°C are obtained. The contact conductance exceeds or is comparable to that of all other TIMs, provided that solder reflow has occurred and the composite thickness is ≤100 μm. Upon decreasing the thickness below 100 μm, the sandwich thermal resistivity decreases abruptly, the composite through-thickness thermal conductivity increases abruptly to values comparable to the calculated values based on the rule of mixtures (parallel model), and the composite–copper interfacial thermal resistivity (rather than the composite resistivity) becomes dominant.

Key words: Thermal interface material, solder, tin, network, exfoliated graphite, thermal contact

INTRODUCTION

A thermal interface material (TIM) is a material positioned at the interface between two surfaces for improving the thermal contact between the surfaces.[1] This is particularly needed in microelectronics, where heat dissipation is a serious problem that limits performance, reliability, and further miniaturization. In a microelectronic package, the two surfaces can be the heat sink and the microprocessor, for example.

A form of TIM is a thermal paste, which typically comprises particles and an organic vehicle. The particles are preferably those that exhibit substantial thermal conductivity. Due to the fact that the adjoining surfaces are never perfectly smooth, the ability of the paste to conform to the topography of the adjoining surfaces is very important. Inadequate conformability will result in air pockets at the interface, thus adversely affecting the quality of the thermal contact. For the sake of conformability, the vehicle should be sufficiently fluid. Silver particles,[2,3] carbon black,[4–6] and graphite nanoplatelets[7,8] are effective particles for formulating thermal pastes. Due to the attraction of a paste that is electrically nonconductive, zinc oxide particles[9] and fumed alumina particles[10] are also used to formulate thermal pastes. Carbon black and fumed alumina have the particular advantage of compressibility (squishability), which results from the fact that they are in the form of porous aggregates of nanoparticles.

(Received June 4, 2014; accepted December 9, 2014; published online January 8, 2015)

Another form of TIM is a sheet, which is used in place of a thermal paste when there is a gap that needs to be filled between the two adjoining surfaces and/or when the handleability provided by a sheet is desired. An example of such a sheet is aluminum foil that has been coated with a thermal paste on both sides.[11] Another example is an elastomer-matrix composite that contains a thermally conductive filler.[11] The most common elastomer is silicone. Yet another example is a carbon nanotube array, with the direction of the nanotubes being perpendicular to the plane of the sheet.[12–20] However, carbon nanotube arrays suffer from high material cost and processing complexity, which stems from the fact that the nanotubes need to grow from a suitable substrate at a sufficiently high temperature. Due to the large thickness of a thermal interface sheet (e.g., 7 μm to 510 μm[11]) compared with a layer of thermal paste (e.g., 0.2 μm to 7 μm[21]), high thermal conductivity in the through-thickness direction of the sheet is more important for a thermal interface sheet than a thermal paste. Achieving high thermal conductivity has been a challenge for all these sheets.

Yet another example of a thermal interface sheet is "flexible graphite," which is formed by compaction of exfoliated graphite particles. Exfoliated graphite is typically formed by exfoliation of intercalated graphite flakes.[22–24] Exfoliation involves expansion by up to hundreds of times along the *c*-axis of the graphite flake and is most commonly performed by rapid heating. Because of the cellular structure of exfoliated graphite, compaction of a collection of exfoliated graphite results in mechanical interlocking of the exfoliated graphite particles, thereby forming a sheet. This sheet is resilient in the direction perpendicular to the sheet, due to the cellular structure of exfoliated graphite and the preferred orientation of the graphite layers in the plane of the sheet.[25–27] The sheet is known as "flexible graphite."[28,29] The resiliency helps the conformability, though the conformability of flexible graphite is low compared with that of high-performance thermal paste. The through-thickness thermal conductivity is low,[25,30] due to the preferred orientation of the graphite layers of the flexible graphite in the plane of the sheet. Mats made of a combination of exfoliated graphite nanoplatelets, carbon nanotubes, and carbon nanofibers have been reported to provide thermal contact conductance of 2×10^4 W/(m^2 K).[31] This value is low compared with the value of up to 26×10^4 W/(m^2 K) provided by graphite nanoplatelet paste.[7] Vertically aligned carbon nanotubes have been grown on flexible graphite, but the performance for this material as a TIM between two surfaces has not been evaluated.[32]

Solders have long been used as TIMs.[33] Voiding has been a major issue in solders. The thermal resistance of soldered joints is increased by the formation of voids, which can occur both in the solder and at the interface between solder and the adjoining surface.[34] Moreover, in case of tin-containing solders interfacing with a copper surface, the tin in the molten solder reacts with copper to form intermetallic compounds.[35] The compounds hinder the ability of the molten solder to wet the copper surface. Furthermore, cracks tend to form at the interface between tin and the compound.

Fillers[36–41] have been added to solders to form solder-matrix composites that exhibit decreased values of coefficient of thermal expansion (CTE) and/or enhanced creep resistance. Graphite particles (100 nm to 500 nm) up to 70 vol.% have been added to tin in order to reduce the CTE;[38] nanosized graphite (400 nm size) has been added to Sn-Bi solder in order to improve the creep resistance, but the addition harms the spreadability of the solder;[39] copper particles have been added to Sn-Zn solder for improving the creep resistance;[40] carbon nanotubes have been added to Sn-Ag-Cu solder for decreasing the CTE, improving the thermal stability, and decreasing the intermetallic compound thickness.[36,41] By incorporating 29 vol.% continuous copper-plated carbon fibers in 60Sn-40Pb solder, the CTE is lowered from 24×10^{-6}/°C to 8×10^{-6}/°C.[37] In spite of the improved relevant properties rendered by the filler or continuous fiber incorporation, the effectiveness of solder-matrix composites as TIMs has not been previously evaluated.

A laminate of nickel-coated flexible graphite sheets bonded with electroplated 96.5Sn-3.5Ag solder, such that the solder content in the laminate is 9 vol.% to 11 vol.%, exhibits an in-plane CTE of -0.2×10^{-6}/°C (slightly negative, essentially zero) and in-plane thermal contact conductance (with the laminate oriented with the in-plane direction being vertical when the laminate is positioned between horizontal sandwiching surfaces) up to 29×10^4 W/(m^2 K), provided that the solder in the laminate is melted during the TIM installation.[42,43] The essentially zero value of the CTE is too low for matching with the CTE of ceramics or semiconductors encountered in electronic packages.

Metal (copper or silver) particles have been added to isotropic graphite to improve the thermal conductivity.[44] However, the nonconformability of the resulting graphite-matrix composite is not attractive for use as a TIM.

In contrast to the laminate structure of prior work,[42,43] this work combines solder with exfoliated graphite, such that the resulting structure is a solder–graphite composite with both solder and graphite exhibiting a degree of networking and with the two networks interpenetrating. Due to the compression of the exfoliated graphite during composite fabrication, flexible graphite is formed within the graphite network. The networking of the solder, as enabled by molten solder flow, promotes thermal conductivity, which is inadequate in unmodified flexible graphite in the through-thickness direction.[45] This work is aimed at (i) the development and fabrication of a composite material with the

above-mentioned novel structure, (ii) investigation of the performance of the developed material as a TIM, and (iii) comparison of the TIM performance of this material with other materials.

Meaningful comparison of the performance of various TIMs should be conducted for the same composition and roughness of the sandwiching surfaces; For example, decrease of the roughness from 15 μm to 0.05 μm increases the thermal contact conductance of a carbon black paste between copper surfaces from 9×10^4 W/(m^2 K) to 29×10^4 W/(m^2 K).[5] The pressure applied to the thermal contact in the direction perpendicular to the plane of the contact is another parameter that should be controlled. Thus, in relation to the third objective, this work compares TIMs that are tested using the same technique under identical conditions. The comparison involves a large variety of TIMs, due to the extensive prior work of one of the authors (D.D.L.C.).[1–7,10,11,20,21]

EXPERIMENTAL PROCEDURES

Materials

Two types of solder powder (a lead-containing solder and a lead-free solder) were used. The lead-containing solder was 63Sn-37Pb (referred to as type A), which is one of the most commonly used solders and is a eutectic solid with a low melting point of 183°C.[46] The lead-free type of solder was 95.5Sn-4Ag-0.5Cu (referred to as type B), which is nearly eutectic in composition with a melting point ranging from 217°C to 219°C.[46] The melting point is higher for type B than type A. Both types of solder powder were provided by Heraeus Materials Technology GmbH & Co, Potsdam, Germany. For both types, the powder particles were spherical in shape, with typical diameter around 6 μm to 8 μm, as shown by optical microscopy.

Exfoliated graphite was formed by rapid heating of sulfuric-acid-intercalated graphite flakes. The flakes had typical mean size of 0.25 mm (65% on 80 mesh) and specific volume of 1.25 cm^2/g. The intercalated graphite flake used in this work is designated as grade 3772, supplied by Asbury Carbons, Asbury, NJ. The expandable flake graphite was contained in stainless-steel foil tubing of length 65 cm and then heated in a crucible resistance furnace (Thermcraft) for 2 min at 900°C with nitrogen purging.

A worm refers to the exfoliated graphite obtained from a single graphite flake. Each worm has length 2 mm to 4 mm and specific surface area 41 m^2/g (measured by nitrogen adsorption, using a Micromeritics ASAP 2010 instrument). Each worm exhibits a cellular structure (Figs. 1 and 2), such that the cell wall consists of about 60 graphite layers, as determined based on the measured specific surface area. During exfoliation, the cell wall extends greatly like a balloon due to extensive sliding between the graphite layers in the cell wall.

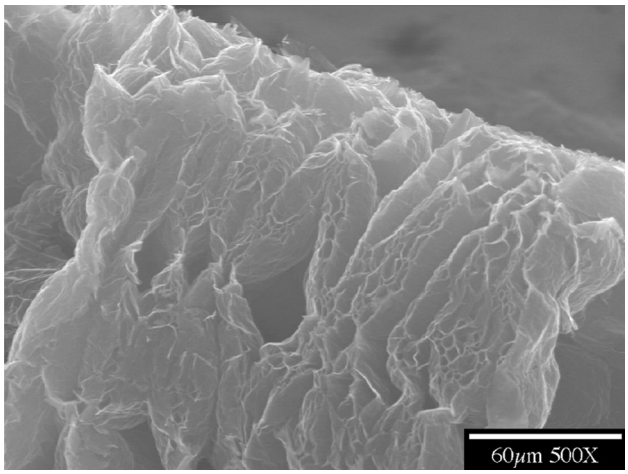

Fig. 1. SEM image of exfoliated graphite used in this work, showing the well-known cellular microstructure. A worm is a piece of exfoliated graphite obtained by exfoliation of a single graphite flake. Only a part of a worm is shown. Exfoliation was conducted by rapid heating of acid-intercalated graphite flakes.

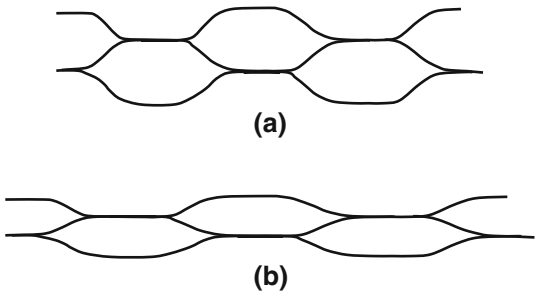

Fig. 2. Schematic illustration (not to scale) of the cellular structure of exfoliated graphite. The cell wall, which is a nanoscale multilayer that consists of about 60 graphite layers, can stretch greatly due to the sliding of the graphite layers with respect to one another. The solid line denotes the cell wall. The individual layers in the multilayer are not shown. (a) Before loading. (b) During loading.

The ease of sliding between the graphite layers in a cell wall after exfoliation is enabled by the loosening of the interlayer interface that occurred during exfoliation. Due to this sliding, the cell wall is strongly viscous.[47,48]

Due to the cellular structure of each worm, compression of a collection of worms in the absence of a binder results in mechanical interlocking among the worms, thereby forming a sheet (flexible graphite). Because of the high degree of compaction during the compression of the worms, the resulting flexible graphite exhibits preferred crystallographic orientation of the graphite layers in the plane perpendicular to the direction of compression during fabrication. The greater the compression pressure, the higher the degree of preferred orientation.[25] Due to the viscous behavior of the cell wall and the preferred orientation of the graphite layers, the flexible graphite sheet is resilient in the through-thickness direction. The resiliency enhances the

Table I. Basic technical data for the solders (without graphite) and flexible graphite (without solder and fabricated at the same pressure as in this work)

Material	Density (g/cm^3)	Electrical conductivity (Ω^{-1} cm^{-1})	Thermal conductivity [W/(m K)]	CTE (/°C)
Solder A	8.40[46]	6.8×10^4 [46]	50[46]	24.00×10^{-6} [46]
Solder B	7.44[46]	7.5×10^4 [46]	62[46]	21.40×10^{-6} [46]
Flexible graphite	0.82[25]	1.3×10^{3a} [47] 23.8[b] [45]	5.8[b] [50]	-0.4×10^{-6a} [49]

[a]In-plane direction.[b]Through-thickness direction.

conformability, which is important for the performance of a thermal interface material.

The basic technical data for unmodified flexible graphite (without solder) and both types of solder are summarized in Table I. Solder A (with lead) exhibits lower thermal and electrical conductivities and higher CTE and density than solder B (lead-free). The higher CTE of solder A is consistent with the lower melting temperature of solder A. The thermal and electrical conductivities of either type of solder are higher than those of flexible graphite, as expected.

Surface treatment of the worms was performed in order to enhance the wettability of the worms by the molten solder. Ozone treatment of graphite is a process of surface oxidation that results in oxygen-containing functional groups on the graphite surface, thereby promoting wetting.[51] The ozone treatment involved exposure of the worms to ozone gas (1 vol.%) for 25 min at 160°C. An ozone generator (Ozonology) was used to produce ozone from oxygen. The heating was provided by a resistance tube furnace (Lindberg). Ozone-treated worms were used in this work, unless noted otherwise.

In this work, the worms and solder particles were dry-mixed in a closed bottle by manual shaking for 30 min, such that the shaking involved agitation by manual 180° reversal of the orientation of the bottle thousands of times. The mixture was then compressed in a stainless-steel mold of diameter 31.7 mm (1.25 inches) at pressure of 11.2 MPa for 5 min. Due to the cellular structure of exfoliated graphite, the compression step causes mechanical interlocking between the worms and hence the formation of a graphite network, which coexists with the distributed solder particles. The solder particles are not located within the pores of a worm, but are located among the worms.

The proportion of solder to graphite in the resulting solder–graphite composite is controlled by the ratio of the masses of solder and worms in the mixture. The density of the graphite in the resulting composite (after the entire fabrication process) was taken as 0.82 g/cm^3 (Table I). The heating that followed the compression was performed in two steps in a hydraulic hot press (Carver, with steel platens sandwiching the specimen mold) used without pressure application. In the first step (the preheating), the mold along with the mixture was heated at 215°C (for type A) or 250°C (for type B) for 80 min in the absence of pressure application for the purpose of melting the solder. These temperatures are above the respective melting temperatures of solder types A and B. For both types of solder, the occurrence of melting was confirmed by seepage of a small amount of solder from the mold. After heating for 80 min, pressure of 11.2 MPa was applied for 4 min in order to promote spreading of the molten solder, and then the furnace was allowed to cool to room temperature. In the second step (the reheating), the composite formed was reheated above the melting temperature of the respective solder, again at 215°C for type A and 250°C for type B, for 60 min. Immediately after this and with the temperature maintained, a pressure of 1.1 MPa was applied for 2 min. Then, the furnace was allowed to cool to room temperature. The reheating serves to further enhance the spreading of the molten solder. For specimens used for measuring the thermal contact conductance while the specimen is sandwiched by copper surfaces, the reheating took place with the specimen sandwiched by two copper cylinders, which are parts of the guarded hot plate apparatus (see "Measurement of Thermal Contact Conductance" section). In other words, the reheating occurred during the formation of the thermal interface. Unless noted otherwise, this reheating was performed for all the solder-containing TIMs of this work. For specimens used for all other tests, the reheating took place in the stainless-steel mold mentioned above in the absence of the copper cylinders. No flux was used.

Measurement of Thermal Contact Conductance

One of the most common and reliable methods for measurement of thermal contact conductance is the guarded hot plate method (ASTM method D5470),[5,11] which is a steady-state method. This method involves measurement of the thermal resistance at thermal equilibrium between a hot

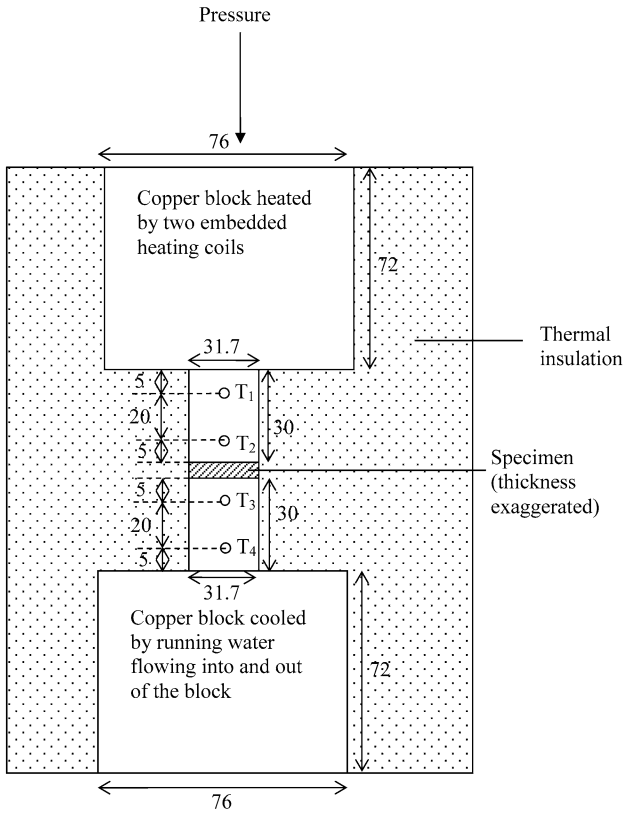

Fig. 3. Schematic illustration of the guarded hot plate experimental setup for measurement of thermal contact conductance. The specimen is sandwiched by two copper cylinders, and the temperature gradient is measured by measuring the temperatures T_1, T_2, T_3, and T_4. All dimensions in millimeters.

surface and a cold surface that sandwich a specimen. The measured thermal resistance consists of the thermal resistance of the specimen and that of each of the two interfaces, such that each interface is that between the specimen and a sandwiching surface. The composition and roughness of the surfaces and the pressure applied to the thermal contact in the direction perpendicular to the contact affect the thermal contact conductance, so these quantities need to be controlled for the sake of meaningful comparison of the thermal interfacing effectiveness of different specimens.

In this work, two copper cylinders were used to sandwich the specimen to be tested for its effectiveness as a TIM between the two copper surfaces (Fig. 3). Each copper surface had roughness of about 15 μm, as provided by mechanical polishing using 600-grit sandpaper, which was also used lightly, as necessary, to remove any surface contaminant (e.g., oxides) that may be present after a test. This level of roughness is the same as that of prior work that referred to this as the "rough" case.[5,11]

Each copper cylinder had height of 30.0 mm and diameter of 1.25 inches (31.7 mm). Each cylinder had two drilled blind holes (3.3 mm diameter) for inserting a thermocouple. The center of each circular hole was 5.0 mm from an end surface of the cylinder. The two holes in each cylinder along with the thermocouple allowed measurement of the temperature gradient in this cylinder. Based on the temperature gradient, the temperature at the end surface of the cylinder touching the specimen could be obtained by extrapolation. The temperatures at the bottom surface of the specimen and the top surface of the bottom copper cylinder are the same. Similarly, the temperatures at the top surface of the specimen and the bottom surface of the top copper cylinder are the same. Thus, the temperature gradient across the specimen thickness was determined.

A temperature gradient was imposed between the copper cylinders by the use of two larger, 3.00 inch × 3.00 inch (76.0 mm × 76.0 mm) square copper blocks. The block above the top copper cylinder served as a heat source, as it had embedded heating coils, such that the temperature was controlled by using a temperature controller, with the temperature set at 100°C. The block below the bottom copper cylinder served as a cold block, as it was cooled by running water that flowed into and out of the block. In order to minimize heat loss in the direction transverse to the imposed temperature gradient, thermal insulation was provided by wrapping the entire region consisting of the specimen edge, cylinders, and blocks with layers of tight-fitting felt cloth. Thus, the heat flow was essentially one-dimensional. Thermal equilibrium was attained when the temperature at each hole became stable. The entire equilibrium process took about 1.0 h.

A contact pressure (either 0.46 MPa or 0.92 MPa, as in prior work,[5,11] unless stated otherwise) was applied on the thermal interface (between the copper cylinders sandwiching the specimen) in the direction perpendicular to the plane of the interface by a screw-action load cell. The pressure was monitored by using a calibrated attached strain gauge.

For the one-dimensional heat flow in the present situation, the heat flow was the same in all parts of the conduction path, so it could be obtained from that in a copper cylinder. The heat flow q in a copper cylinder with thermal conductivity k and cross-sectional area A due to a temperature gradient $\Delta T/d_A$ is given by

$$q = \frac{\Delta Q}{\Delta t} = \frac{kA\Delta T}{d_A}, \tag{1}$$

where Q is the heat that flows over a time period Δt, d_A is the distance (20.00 mm) between two holes in the cylinder, and ΔT is the temperature difference between these holes.

The temperature at the bottom surface of the top copper cylinder is given by the expression

$$T_A = T_2 - \frac{d_B}{d_A}(T_1 - T_2), \tag{2}$$

where d_B is the distance between the top surface of the specimen and the thermocouple T_2 (5.00 mm)

and d_A is the distance between thermocouple T_1 and T_2 (20.00 mm). Hence, $T_1 - T_2$ is the temperature difference over the distance d_A.

Similarly, the temperature at the top surface of the bottom copper cylinder is given by the expression

$$T_D = T_3 + \frac{d_D}{d_C}(T_3 - T_4), \tag{3}$$

where d_D is the distance between the bottom surface of the specimen and the thermocouple T_3 (5.00 mm) and d_C is the distance between thermocouple T_3 and T_4 (20.00 mm). Hence, $T_3 - T_4$ is the temperature difference over the distance d_C. Since the two copper cylinders are identical, d_C is equal to d_A.

Because of the geometric symmetry of the two copper cylinders, Eqs. 2 and 3 can be simplified to

$$T_A = T_2 - \alpha\Delta T \tag{4}$$

and

$$T_D = T_3 + \alpha\Delta T, \tag{5}$$

where

$$\alpha = \frac{d_B}{d_A} = \frac{d_D}{d_C} = 0.25.$$

The thermal resistivity is given by

$$\theta = (T_A - T_D)\frac{A}{q}. \tag{6}$$

By subtracting Eq. 5 from Eq. 4, substituting the result into Eq. 6, and then substituting q from Eq. 1 into Eq. 6, the thermal resistivity is obtained as

$$\theta = \left(\frac{T_2 - T_3}{\Delta T} - 2\alpha\right)\frac{d_A}{k}. \tag{7}$$

The thermal resistivity is independent of the area, whereas the thermal resistance depends on the area. The reciprocal of the thermal resistivity gives the thermal contact conductance.

Measurement of Through-Thickness Thermal Conductivity

The thermal conductivity is a material property and is to be distinguished from the thermal contact conductance, which describes the effectiveness of heat transfer across the surfaces that sandwich the specimen. The total thermal resistance R_t is given by

$$R_t = R_s + 2R_i, \tag{8}$$

where R_s is the thermal resistance of the specimen and R_i is the thermal resistance of the interface between the specimen and a sandwiching surface. The total thermal resistance is the inverse of the thermal contact conductance divided by the area of the heat conduction path, A. The thermal resistance R_s of the specimen can be written as

$$R_s = \frac{L}{kA}, \tag{9}$$

where k is the thermal conductivity of the specimen and L is the specimen thickness. Therefore, Eq. 8 can be written as

$$R_tA = \frac{L}{k} + 2R_iA. \tag{10}$$

Thus, k is given by the inverse of the slope of a plot of thermal resistivity versus specimen thickness.

Measurement of In-Plane Coefficient of Thermal Expansion

A PerkinElmer Corporation (Norwalk, CT) series 7 thermal analysis system was used for measuring the CTE in the plane perpendicular to the compression direction during specimen fabrication. The measurement was made over the temperature range of 20°C to 100°C. Because of the very low CTE of quartz, a quartz cylindrical probe of 4.0 mm diameter was used to contact the upper surface of the specimen, so that the displacement of the probe indicated the change in thickness of the specimen under the probe. Due to the proximity to room temperature, the temperature of the furnace was controlled partly by a continuous supply of running cold water. The specimen was 5.0 mm long, 3.5 mm wide, and 0.50 mm thick. For controlling the contact between the specimen and the probe, a very small normal force of 10 mN was applied by the probe on the 3.5 mm × 0.50 mm surface of the specimen, so that the dimensional change was measured along the 5.0 mm length of the specimen. Heating and cooling were conducted at a rate of 5°C/min. The specimen was first heated from 20°C to 100°C, then cooled from 100°C to 20°C, then reheated from 20°C to 100°C. The first cycle of heating and cooling was conducted in order to remove any thermal stress. The CTE was obtained from the data during the reheating. The dimensional change during the heating was up to 0.51 μm. Due to the small change in dimension, there was no buckling in the specimen.

Measurement of In-Plane Electrical Conductivity

The in-plane electrical conductivity of the specimens was measured using the four-probe method. This method utilizes four electrical contacts. The outer two contacts (25.0 mm apart) are for passing the current, while the inner two contacts (20.0 mm apart) are for voltage measurement. The electrical contacts were in the form of silver paint in conjunction with tin-coated copper wires of 0.13 mm

diameter. Each contact was around the entire perimeter in a plane perpendicular to the direction of resistance measurement. The specimen was 30.0 mm long (the direction of resistance measurement), 5.0 mm wide, and 0.50 mm thick. A high-precision digital multimeter (Keithley 2001) was used for the direct-current (DC) resistance measurement.

Measurement of Through-Thickness Electrical Conductivity

The measurement of through-thickness electrical conductivity also involved the use of the four-probe method. The specimen was a circular disc of diameter 31.7 mm and thickness 0.50 mm (500 μm). Each of the top and bottom surfaces of the specimen had a current contact and a voltage contact. The current contact on both surfaces was made of a piece of copper foil (thickness 0.15 mm) cut in the shape of a ring with outer diameter being the same as that of the specimen (31.7 mm) and inner diameter being 15.0 mm. The voltage contact on either surface was made of copper foil cut into a circular disc of diameter 10.0 mm, as illustrated in Fig. 4. All the contacts were applied to the specimen by using silver paint between the specimen and the copper foil. Each contact had an integral leg that protruded to facilitate electrical connection. A high-precision multimeter (Keithley 2001) was used for the resistance measurement.

Microscopy

Microscopic examination was conducted by scanning electron microscopy (SEM) on the as-is surface of the composite in the plane of the composite sheet and on the edge fracture surface obtained by flexural fracture of the composite.

RESULTS AND DISCUSSION

In-Plane Electrical Conductivity

The in-plane electrical conductivity was calculated by using the rule of mixtures for resistors in parallel, using the conductivities of the resistors involved as shown in Table I. Table II shows that the measured in-plane electrical conductivity and the ratio of the measured to calculated values of this conductivity were both higher for the composites made with worms that have been ozone treated than those made with worms that have not been treated. In particular, the ozone treatment increases the conductivity ratio from 0.58 to 0.85. This suggests better connectivity of the solder achieved with worms that have been ozone treated. The better connectivity of the solder is probably due to the enhanced wetting of the molten solder on the graphite due to the treatment.

Table III presents the measured and calculated values of the in-plane electrical conductivity, and the ratio of the measured conductivity to the calculated conductivity for solder A and solder B composites at various solder volume fractions. For either type of solder, the measured conductivity increased monotonically with increasing solder content, such that it abruptly increased at solder content around 55 vol.% to 56 vol.% (Table III). The ratio of the measured conductivity to the calculated conductivity also increased monotonically with increasing solder content, such that it abruptly increased at a solder content around 55 vol.% to 56 vol.% (Table III; Fig. 5). This means that the parallel resistor model becomes more accurate at solder contents above 55 vol.% to 56 vol.%, due to better solder connectivity above 55 vol.% to 56 vol.%. As a consequence, the measured conductivity is much below the calculated value below 55 vol.% and approaches 1 at the highest solder content of 65 vol.%. Therefore, the solder content of 55 vol.% to 56 vol.% was chosen for subsequent investigation.

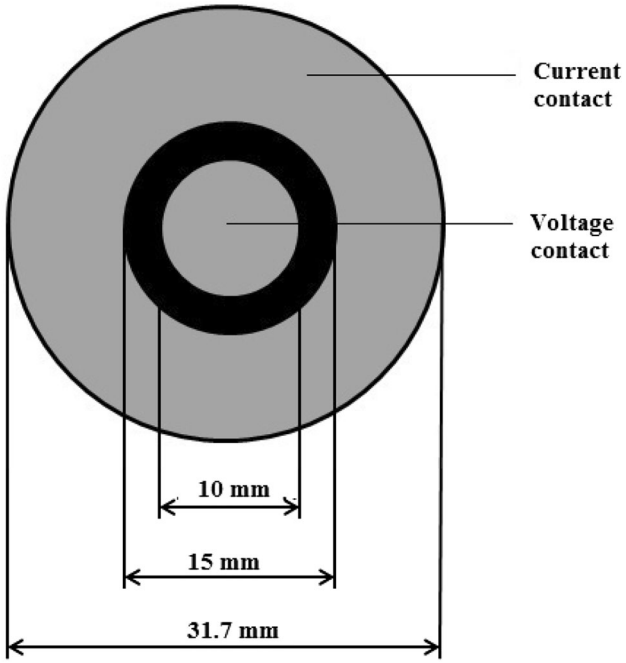

Fig. 4. Electrical contact configuration for measuring the through-thickness electrical conductivity using the four-probe method. The grey regions are electrical contacts. The outer contact is for passing current. The inner contact is for voltage measurement. The black region is the part of the specimen surface that is not covered by any electrical contact.

At the same solder content in the range ≥50 vol.%, type A solder gave a lower conductivity and a lower ratio of the measured conductivity to the calculated conductivity than type B solder (Table III). Unless stated otherwise, testing was conducted on type A solder composite containing 55 vol.% solder and type B solder composite containing 56 vol.% solder.

The higher conductivity for solder B composites is consistent with the higher conductivity of solder B than solder A in the absence of graphite (Table I). The higher ratio for type B indicates that the

Table II. Effect of ozone treatment of the worms on the in-plane electrical conductivity of solder–graphite composites made with type A solder

Vol.% Solder	Ozone Treatment	Measured Conductivity ($10^4\ \Omega^{-1}\ cm^{-1}$)	Calculated Conductivity ($10^4\ \Omega^{-1}\ cm^{-1}$)	Measured Conductivity/Calculated Conductivity
55	Yes	3.29 ± 0.05	3.86	0.85 ± 0.01
56	No	2.24 ± 0.08	3.90	0.58 ± 0.02

Table III. Variation of in-plane electrical conductivity with solder volume fraction

Solder Type	Solder Vol.%	Electrical Conductivity ($10^4\ \Omega^{-1}\ cm^{-1}$)		Ratio of Measured Conductivity to Calculated Conductivity
		Measured	Calculated	
A	35	0.40 ± 0.02	2.51	0.16 ± 0.01
	42	0.63 ± 0.06	2.98	0.21 ± 0.02
	50	1.18 ± 0.03	3.52	0.34 ± 0.01
	55	3.29 ± 0.05	3.86	0.85 ± 0.01
	60	3.60 ± 0.01	4.19	0.86 ± 0.00
	65	3.90 ± 0.03	4.53	0.86 ± 0.01
B	31	0.42 ± 0.05	2.44	0.17 ± 0.02
	38	0.55 ± 0.01	2.97	0.19 ± 0.00
	50	1.82 ± 0.04	3.86	0.47 ± 0.01
	56	3.87 ± 0.04	4.30	0.90 ± 0.01
	62	4.29 ± 0.02	4.75	0.91 ± 0.00
	65	4.59 ± 0.03	4.97	0.92 ± 0.01

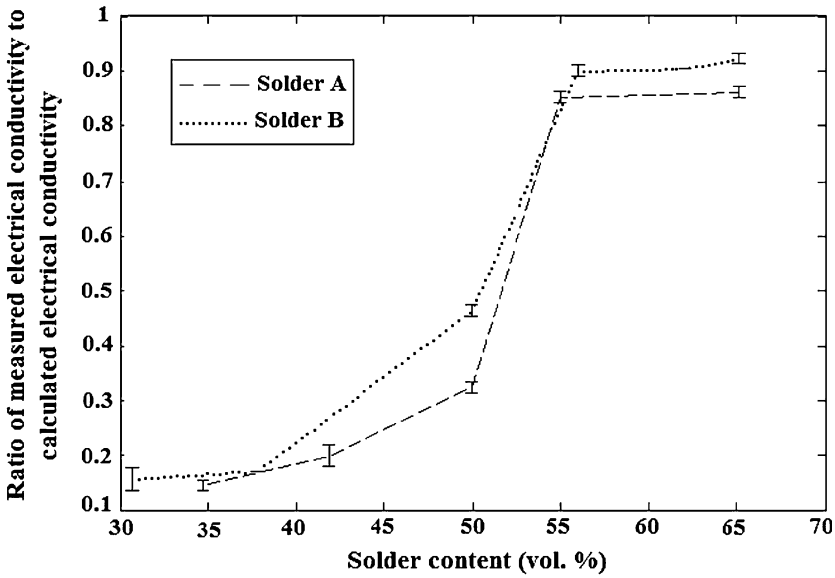

Fig. 5. Variation of the ratio of measured to calculated in-plane electrical conductivity with solder content.

Table IV. Through-thickness electrical conductivity for thickness of 500 μm

Solder Type	Measured Electrical Conductivity ($10^4\ \Omega^{-1}\ cm^{-1}$)	Calculated Electrical Conductivity ($10^4\ \Omega^{-1}\ cm^{-1}$)		Ratio of Measured Conductivity to Calculated Conductivity		Ratio of In-Plane Electrical Conductivity[a] to Through-Thickness Conductivity
		Based on Resistors in Parallel	Based on Resistors in Series	Calculation Based on Resistors in Parallel	Calculation Based on Resistors in Series	
A	0.44 ± 0.05	3.74	0.30	0.12 ± 0.01	1.47 ± 0.16	7.48 ± 0.98
B	0.53 ± 0.02	4.13	0.31	0.13 ± 0.00	1.71 ± 0.06	7.30 ± 0.36

Solder content was 55 vol.% and 56 vol.% for type A and type B composites, respectively. [a]From Table III.

electrical connectivity of the solder is superior for solder B than solder A.

Through-Thickness Electrical Conductivity

The through-thickness electrical conductivity (Table IV) was much lower than the in-plane electrical conductivity (Table III). The ratio of the in-plane conductivity to the through-thickness conductivity was 7, suggesting substantial preferred orientation of the graphite layers in the in-plane direction (as for flexible graphite in the absence of solder). This also reflects the poor electrical connectivity of the solder in the through-thickness direction compared with the in-plane direction. The calculated through-thickness electrical conductivity based on resistors in series was closer to the measured value than that based on resistors in parallel. This further supports the notion that the electrical connection of the solder is poor in the through-thickness direction. However, the measured conductivity was between the calculated values based on the parallel and series models, indicating that there is still a degree of connectivity of the solder in the through-thickness direction. The ratio of the measured conductivity to the calculated conductivity (based on resistors in series) was higher for type B than type A, suggesting better through-thickness solder connectivity for type B.

For the same solder content of 55 vol.% to 56 vol.% and the same thickness of 500 μm, the through-thickness electrical conductivity was higher for the solder B composite than the solder A composite. This is consistent with the higher conductivity of solder B in the absence of graphite (Table I).

In-Plane Coefficient of Thermal Expansion

The in-plane CTE was below 13×10^{-6}/°C for both solder A and solder B composites containing 55 vol.% to 56 vol.% solder, as shown in Table V. The composites provided 47% and 52% reductions in the CTE value compared with the solder itself for type A and type B solder, respectively. The measured CTE value was lower for the solder B composite than the solder A composite. This is consistent with the fact that the CTE of the solder in the absence of graphite was lower for solder B than solder A (Table I). The calculated values are based on the rule of mixtures, using the volume fractions of the components as the weighting factors and the CTE values of the components shown in Table I. The ratio of the measured CTE to the calculated CTE was close to 1 for both solder A and solder B composites, but the ratio was slightly higher for the solder A composite. This probably reflects the lower degree of in-plane connectivity of the solder in the solder A composite (as shown by the in-plane electrical conductivity measurement in "In-Plane Electrical Conductivity" section) and the consequent

Table V. CTE of solder–graphite composites

Solder Type	Measured CTE (10^{-6}/°C)	Calculated CTE (10^{-6}/°C)	Ratio of Measured CTE to Calculated CTE
A	12.66 ± 0.03	13.02	0.97 ± 0.00
B	10.18 ± 0.04	11.59	0.88 ± 0.00

The solder content was 55 vol.% and 56 vol.% for type A and type B composites, respectively.

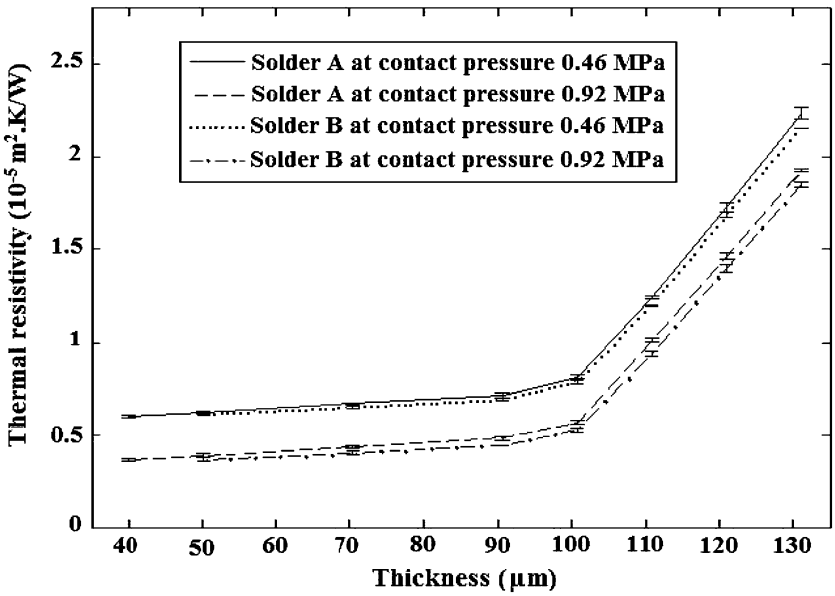

Fig. 6. Variation of total thermal resistivity with specimen thickness. The reciprocal of the thermal resistivity is the thermal contact conductance. The specimens are solder–graphite composites with 55 vol.% to 56 vol.% solder.

Table VI. Composite–copper interfacial thermal resistivity for the solder–graphite composites

	Interfacial Thermal Resistivity [10^{-6} (m^2 K)/W]	
Solder Type	0.92 MPa	0.46 MPa
A	1.43 ± 0.13	2.58 ± 0.13
B	1.42 ± 0.06	2.63 ± 0.03

The solder content was 55 vol.% and 56 vol.% for type A and type B composites, respectively.

larger area of the interface between solder and graphite in the solder A composite.

Thermal Contact Conductance and Specimen–Copper Interfacial Thermal Resistivity

Figure 6 shows the variation of the total thermal resistivity (the product of the thermal resistance and the area) with the thickness for solder A and solder B composites, each tested at two different contact pressures. The specimens contained 55 vol.% to 56 vol.% solder.

Solder A and solder B at the same pressure and the same thickness gave essentially the same value of the total thermal resistivity. For either type of solder and for any of the thicknesses, an increase in pressure from 0.46 MPa to 0.92 MPa decreased the total thermal resistivity. This decrease is due to a decrease in the thermal resistivity of the interface between the specimen and each of the two copper surfaces sandwiching the specimen, as shown in Table VI, where the interfacial thermal resistivity is equal to half of the intercept with the thermal resistivity axis of the curve of the total thermal resistivity (in the small thickness regime) versus thickness (Fig. 6) at zero thickness. Because of the nanoscale structure of the interface region and the possible difference in structure between this region and the bulk material, the value of the interfacial resistivity obtained by this extrapolation method should be strictly speaking considered a nominal value of the interfacial resistivity. Nevertheless, this nominal value is practically useful for describing the behavior of the thermal interface. Furthermore, this value pertains to the small thickness

Table VII. Dependence of thermal contact conductance (reciprocal of total thermal resistivity) on specimen thickness, contact pressure, and solder type

		Thermal Contact Conductance [10^4 W/(m^2 K)]		Fractional Increase in Thermal Contact Conductance[a]		Total Thermal Resistivity [10^{-6} (m^2 K)/W]		Fraction of Total Thermal Resistivity That Is Interfacial[c]	
Thickness (μm)	**Contact Pressure (MPa)**	**Solder A**	**Solder B**	**Solder A**	**Solder B**	**Solder A**	**Solder B**	**Solder A**	**Solder B**
130	0.92	5.19 ± 0.02	5.40 ± 0.05	0.16 ± 0.02	1.16 ± 0.01	19.27 ± 0.07	18.52 ± 0.17	0.15 ± 0.01	0.15 ± 0.01
	0.46	4.48 ± 0.06	4.65 ± 0.00			22.32 ± 0.29	21.51 ± 0.00	0.23 ± 0.01	0.24 ± 0.00
120	0.92	6.81 ± 0.09	7.13 ± 0.11	0.18 ± 0.03	0.21 ± 0.01	14.68 ± 0.19	14.03 ± 0.21	0.20 ± 0.02	0.20 ± 0.01
	0.46	5.78 ± 0.09	5.91 ± 0.05			17.30 ± 0.26	16.89 ± 0.14	0.30 ± 0.01	0.31 ± 001
110	0.92	9.81 ± 0.11	10.53 ± 0.14	0.22 ± 0.02	0.27 ± 0.02	10.19 ± 0.11	9.50 ± 0.12	0.28 ± 0.01	0.30 ± 0.01
	0.46	8.01 ± 0.03	8.30 ± 0.04			12.48 ± 0.05	12.05 ± 0.06	0.41 ± 0.00	0.44 ± 0.01
100	0.92	17.23 ± 0.29	18.48 ± 0.38	0.42 ± 0.01	0.48 ± 0.53	5.80 ± 0.10	5.41 ± 0.11	0.49 ± 0.01	0.52 ± 0.01
	0.46	12.13 ± 0.14	12.51 ± 0.17			8.24 ± 0.09	7.99 ± 0.11	0.63 ± 0.01	0.66 ± 0.01
90	0.92	20.08 ± 0.39	21.84 ± 0.07	0.46 ± 0.05	0.53 ± 0.02	4.98 ± 0.09	4.59 ± 0.01	0.58 ± 0.01	0.62 ± 0.00
	0.46	13.76 ± 0.26	14.25 ± 0.11			7.27 ± 0.13	7.02 ± 0.05	0.71 ± 0.02	0.75 ± 0.01
70	0.92	22.16 ± 0.28	23.84 ± 0.63	0.51 ± 0.02	0.58 ± 0.06	4.51 ± 0.06	4.19 ± 0.11	0.64 ± 0.01	0.67 ± 0.01
	0.46	14.71 ± 0.06	15.08 ± 0.18			6.80 ± 0.03	6.63 ± 0.08	0.76 ± 0.00	0.79 ± 0.01
50	0.92	24.71 ± 0.55	26.19 ± 0.75	0.57 ± 0.04	0.63 ± 0.06	4.05 ± 0.09	3.82 ± 0.11	0.71 ± 0.01	0.74 ± 0.02
	0.46	15.79 ± 0.12	16.04 ± 0.10			6.33 ± 0.05	6.23 ± 0.04	0.81 ± 0.01	0.84 ± 0.00
40	0.92	26.22 ± 0.62	[b]	0.60 ± 0.06	[b]	3.81 ± 0.09	[b]	0.75 ± 0.01	[b]
	0.46	16.39 ± 0.21	[b]			6.10 ± 0.08	[b]	0.85 ± 0.01	[b]

The specimens were solder–graphite composites. The solder content was 55 vol.% and 56 vol.% for type A and type B composites, respectively.[a]Due to increase in contact pressure from 0.46 MPa to 0.92 MPa.[b]Not determined.[c]Interfacial resistivity on both sides of the specimen considered.

Table VIII. Effect of contact pressure on thermal contact conductance for type B solder–graphite composite containing 56 vol.% solder

	Thermal Contact Conductance [10^4 W/(m^2 K)]		
Thickness (μm)	**0.92 MPa**	**0.46 MPa**	**0.00 MPa**
100	18.48 ± 0.38	12.51 ± 0.17	8.63 ± 0.02
50	26.19 ± 0.75	16.04 ± 0.10	9.98 ± 0.04

Table IX. Effect of solder melting on thermal contact conductance for solder–graphite composite containing 56 vol.% type B solder

		Thermal Contact Conductance [10^4 W/(m^2 K)]	
Thickness (μm)	**Solder Melting**	**0.92 MPa**	**0.46 MPa**
90	Yes	21.84	14.25
85	No	1.98	1.41

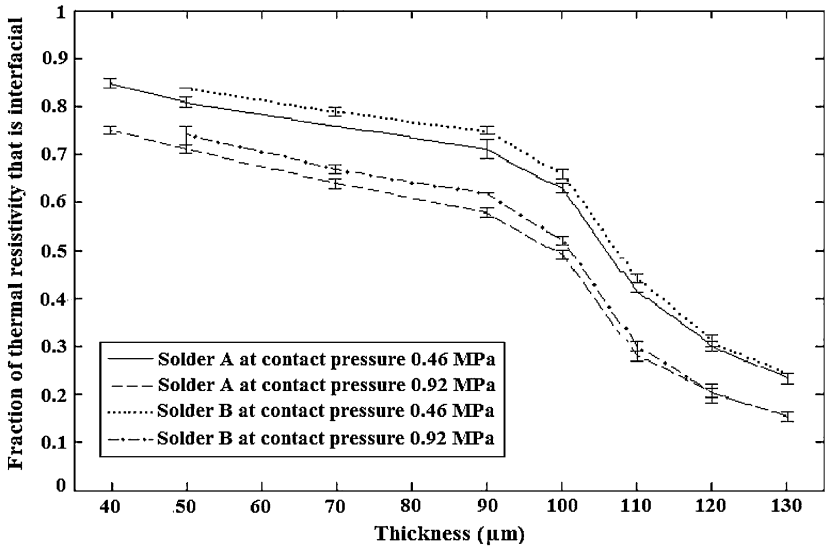

Fig. 7. Variation in contribution of interfacial thermal resistivity to total (sandwich) thermal resistivity with thickness. The sum of the interfacial resistivity at the top and bottom surfaces is considered. The specimens contained 55 vol.% to 56 vol.% solder.

regime, which is the practically important regime for high TIM performance. As expected, an increase in pressure improves the conformability of the TIM, thereby decreasing the thermal resistivity of this interface (Table VI). For both solder composites (55 vol.% to 56 vol.% solder), each at two contact pressures (0.46 MPa and 0.92 MPa), the interfacial thermal resistivity was lower by an order of magnitude than that previously reported as 54×10^{-6} (m^2 K)/W for unmodified flexible graphite (without solder) fabricated at the same pressure as this work.[50] This means that the addition of solder to flexible graphite significantly decreased the interfacial thermal resistivity through conformability enhancement. Although flexible graphite has a degree of conformability, the molten solder in the composite during TIM installation is the main contributor to the conformability of the TIM.

For any combination of solder and pressure, the curve of thermal resistivity versus thickness was piecewise linear, with two linear segments. The linear segment in the high thickness regime had a higher slope than that in the low thickness regime. An abrupt change in slope occurred at thickness of 90 μm to 100 μm. Since the slope is inversely related to the thermal conductivity of the specimen, the above results mean that, for any combination of solder and contact pressure, the thermal conduc-

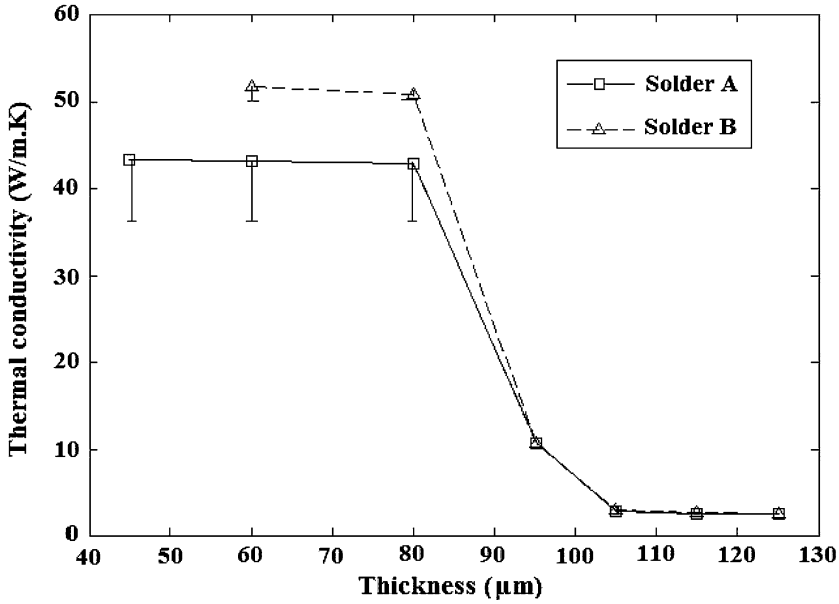

Fig. 8. Variation of through-thickness thermal conductivity with thickness at constant contact pressure of 0.46 MPa. The error bars in the small thickness regime (below 90 μm) show only the lower bounds, because the upper bounds have not been determined. The specimens contained 55 vol.% to 56 vol.% solder.

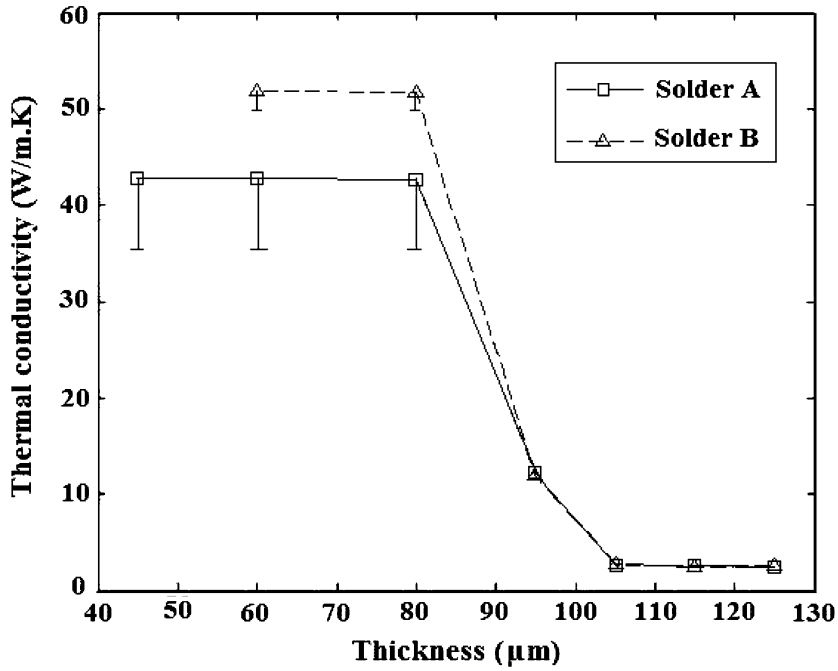

Fig. 9. Variation of through-thickness thermal conductivity with thickness at constant contact pressure of 0.92 MPa. The error bars in the small thickness regime (below 90 μm) show only the lower bounds, because the upper bounds have not been determined. The specimens contained 55 vol.% to 56 vol.% solder.

tivity was lower in the high thickness regime than the low thickness regime.

The thermal contact conductance (the reciprocal of the total thermal resistivity shown in Fig. 6) is presented in Table VII. It decreased monotonically with increasing thickness, such that the decrease was relatively abrupt at thickness 90 μm to 100 μm. For the combination of the smallest thickness of 50 μm and the higher contact pressure of 0.92 MPa, the thermal contact conductance reached 25×10^4 W/(m^2 K) and 26×10^4 W/(m^2 K) for solder A composite and solder B composite, respectively. These values are very high compared with prior work (including prior work on flexible graphite

Table X. Variation of thermal conductivity [W/(m K)] with thickness and contact pressure

Solder Type	Contact Pressure (MPa)	Large Thickness, 100 μm to 130 μm		Small Thickness, 40 μm to 90 μm (solder A) or 50 μm to 90 μm (solder B)		Fractional Increase in Conductivity Due to the Thickness Decrease[a]	Calculated Conductivity	
		Average	Lower Bound	Average	Lower Bound		Parallel Model	Series Model
A	0.46	2.15	2.08	42.7	36.3	19.86	30.11	11.28
	0.92	2.23	2.06	42.7	35.7	19.14		
B	0.46	2.22	2.20	50.6	50.0	22.79	36.71	11.57
	0.92	2.28	2.25	51.9	50.0	22.76		

The upper bound is not available for the case of small thicknesses. There is greater uncertainty for the thermal conductivity in the small thickness regime than the large thickness regime. Thus, only the lower bound can be determined in the small thickness regime. [a]The thickness decrease from the large thickness regime to the small thickness regime.

without solder[50]), as discussed in "Comparison with Prior Work" section.

For the same combination of thickness and contact pressure, the thermal contact conductance tended to be higher for solder B than solder A. This difference became clearer as the thickness was reduced below 100 μm. For the same material and at a given thickness, an increase in the contact pressure increased the thermal contact conductance, such that the effect was more significant at thicknesses ≤100 μm.

Table VIII shows that the thermal contact conductance decreased monotonically as the contact pressure was reduced from 0.92 MPa to 0.46 MPa and to zero, whether the thickness was 100 μm or 50 μm. However, even at zero pressure, the conductance was substantial.

Table IX shows that the absence of solder melting (reheating) during formation of the thermal interface using the solder–graphite composite as a TIM greatly decreased the thermal contact conductance. This means that the melting of the solder is necessary to cause the needed level of conformability of the composite with the sandwiching surfaces.

As the thickness was decreased, the fraction of the total thermal resistivity that was interfacial increased (Table VII; Fig. 7). At thicknesses ≥110 μm, the total thermal resistivity was dominated by the specimen resistivity; at lower thicknesses, the total thermal resistivity was dominated by the interfacial resistivity. This is because of the decrease in the thermal resistance of the specimen as the thickness decreased. This means that, at thicknesses below 110 μm, the conformability of the TIM rather than the thermal conductivity of the TIM governed the TIM performance.

For the same thickness, the fraction of the total thermal resistivity that was interfacial was higher for the lower contact pressure. This is because the interfacial thermal resistivity decreased with increasing contact pressure (Table VI), enhancing the conformability.

Compared with solder itself (without graphite), the solder composite (55 vol.% solder) is attractive for its lower tin content (due to the presence of graphite) and the consequent lower extent of the detrimental tin–copper reaction, which results in intermetallic compounds.[35] In addition, it is attractive for the absence of molten solder seepage, which tends to occur when solder itself (without graphite) is used. Furthermore, the composite is advantageous in that it has a lower CTE (Tables I, V) than the solder by itself.

Through-Thickness Thermal Conductivity

The through-thickness thermal conductivity, as obtained from the slope of the curve of thermal resistivity versus thickness (Fig. 6), is shown in Figs. 8, 9 and Table X. As the thickness increased, the thermal conductivity dropped abruptly at

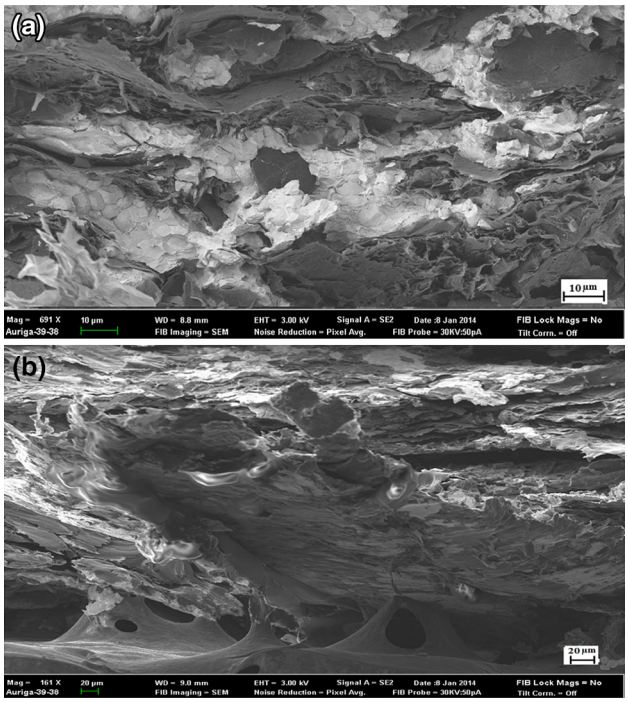

Fig. 10. Scanning electron microscopy images for type A solder composite edge fracture surface view. (a) High magnification (×691). (b) Low magnification (×161). The specimen contained 55 vol.% solder.

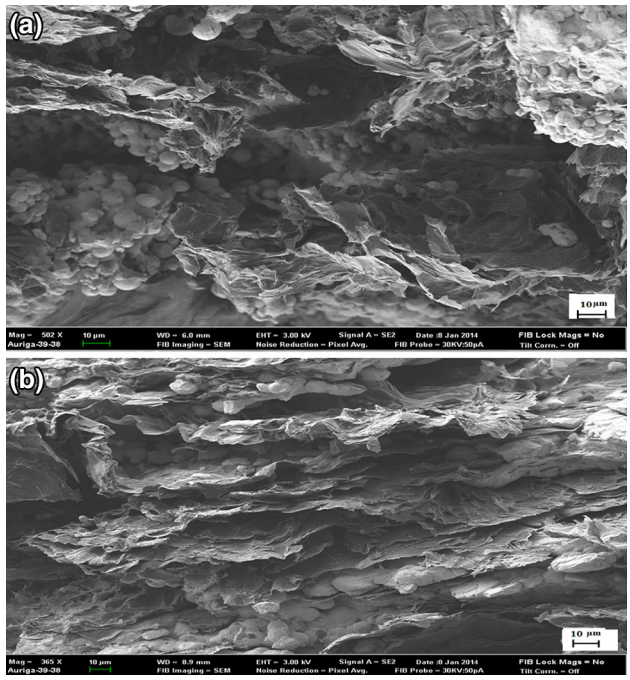

Fig. 11. SEM images for type B solder composite edge fracture surface view. (a) High magnification (×502). (b) Low magnification (×365). The specimen contained 56 vol.% solder.

thickness of 80 μm to 100 μm, such that the thermal conductivity was much higher in the small thickness regime than the large thickness regime. Although the error in the thermal conductivity is relatively large in the small thickness regime, the lower bound of the conductivity in this regime is still high, i.e., 36 W/(m K) and 50 W/(m K) for solder A composite and solder B composite, respectively. These high values indicate that the thermal conductivity was dominated by the solder part of the composite. An increase in the contact pressure had negligible effect on the thermal conductivity (Table X), even though it significantly affected the interfacial thermal resistivity (Table VI).

The thermal conductivity was essentially the same for both types of solder composite at thicknesses above 100 μm. Below thickness of 90 μm, the type B solder composite exhibited higher thermal conductivity than the type A solder composite. This is consistent with the lower thermal conductivity of solder A compared with solder B, both in the absence of graphite (Table I).

The thermal conductivity of a material is a property of the material and should not change with the thickness unless the material structure changes with the thickness. Therefore, the results mean that the structure of the composite exhibits a step change at thickness of 90 μm to 100 μm. This step change in structure is attributed to an increase in the electrical connectivity of the solder in the composite as the thickness is decreased.

The thermal conductivity of flexible graphite in the through-thickness direction decreases with increasing density, which is achieved by increasing the pressure on the worms during fabrication.[25] However, in this work, the fabrication pressure was fixed, so that the density was fixed; the thickness was controlled by the amount of exfoliated graphite used and not by the fabrication pressure. In the absence of solder, the thermal conductivity was 5.8 W/(m K)[50] (Table I), which is higher than those of the solder composites in the large thickness regime and much lower than those of the solder composites in the small thickness regime (Table X).

The thermal conductivity calculated by using the rule of mixtures for thermal resistors in parallel was close to the measured values for the small thickness regime but much higher than those for the large thickness regime. The thermal conductivity calculated for thermal resistors in series was far from the measured values for both the small and large thickness regimes. Thus, the parallel model is superior to the series model for the small thickness regime, whereas the series model is superior to the parallel model for the large thickness regime. This means that the thermal connectivity of the solder in the through-thickness direction was high in the small thickness regime but low in the large thickness regime.

Microstructural Examination

Figure 10 shows scanning electron microscopy (SEM) images of the edge fracture surface (obtained

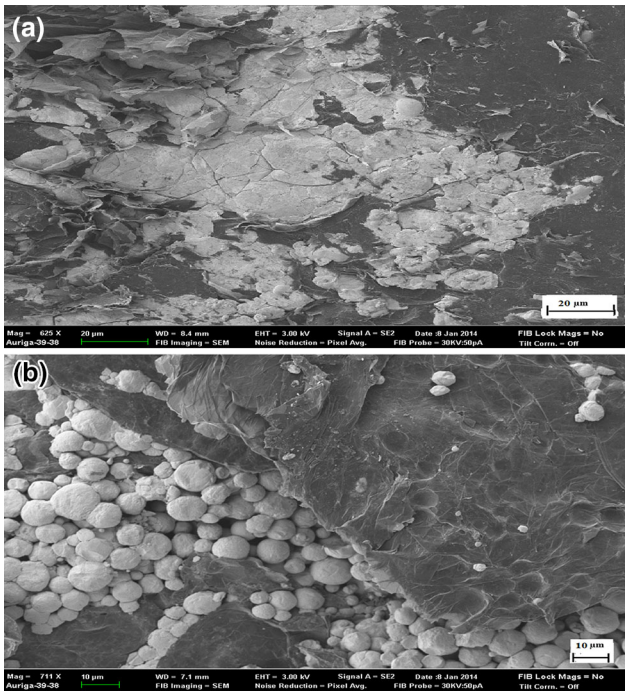

Fig. 12. Scanning electron microscopy in-plane view of (**a**) the type A solder composite and (**b**) the type B solder composite. The specimens contained 55 vol.% to 56 vol.% solder.

by flexure) of the type A solder composite with 55 vol.% solder. The bright regions are solder, and the dark regions are graphite. The graphite exhibits an interconnected layered structure, though the layers are bent. The solder is segregated and is partly in the form of interconnected particles of size similar to that of the solder powder used (Fig. 10a) and partly in the form of a coating on the graphite layers (Fig. 10b). The solder exhibits a degree of three-dimensional connectivity, though the two-dimensional connectivity is stronger.

Figure 11 shows corresponding micrographs for the type B composite. The microstructure is similar to that for the type A composite of Fig. 10. However, the particulate nature of the solder is clearer for the type B composite. The solder particles are more connected for the type A composite than the type B composite. This difference between the two types of solder composite is probably due to the difference in flow behavior between the two types of solder. The flow of the molten solder is apparently limited in case of solder B composite, thus resulting in a particle morphology after melting. The preferred orientation of the graphite layers is clearly shown by Fig. 11b.

Figure 12 shows the in-plane surface microstructure of the solder composites, which are observed without mechanical polishing. The solder in the type A solder composite exists as large patches, though some interconnected solder particles are also observed. In contrast, the solder particles are distinctly observed in the type B solder composite.

Based on the microscopic images, the solder particle connectivity was inferior for type B than type A. However, based on the electrical conductivity results (Tables III, IV), the solder connectivity was slightly superior for type B than type A. Furthermore, the TIM performance, as shown by the thermal contact conductance (Table VII), was slightly better for type B than type A. It is possible that the part of the solder in the form of a coating on the graphite layers is more continuous for the type A composite than the type B composite, as suggested by the greater degree of continuity of the bright regions (which correspond to the solder coating) in Fig. 11b than in Fig. 10b.

In the solder–graphite composites, both solder and graphite exhibit a degree of networking, such that the two networks interpenetrate. The networking in both solder and graphite is indicated by the electrical and thermal conductivity results (Table IV). In addition, the solder networking is supported by the SEM images in Figs. 10a and 12a, and the graphite networking is supported by the SEM images in Figs. 10b and 11b. Further work is needed to examine and understand the structure of the composites of this paper.

Comparison with Prior Work

Table XI shows a comparison of the thermal contact conductance between the solder and solder–graphite composites of this work and various TIM materials (prior work of one of the authors, i.e., D.D.L.C.[2,3,5–7,10,50]) also tested between copper surfaces with the same surface roughness and same contact pressures as in this work. The other TIM materials include thermal pastes, unmodified flexible graphite, thermal-paste-penetrated flexible graphite, thermal-paste-coated flexible graphite, and thermal-paste-coated metal foils. The solder–graphite composite is superior to all the other TIMs listed.

Unmodified flexible graphite has a degree of conformability, but due to its low thermal conductivity in the through-thickness direction, the overall thermal contact conductance is low. At a thickness of 13 μm[11] and a contact pressure of 0.46 MPa, unmodified flexible graphite (commercially available) exhibits a thermal contact conductance of only 1.40×10^4 W/(m^2 K). Despite the high thermal conductivity, unmodified metal foils suffer from low values of the thermal contact conductance due to their poor conformability. Aluminum and copper foils, both 130 μm thick, give thermal contact conductance values of 0.99×10^4 W/(m^2 K) and 0.75×10^4 W/(m^2 K), respectively.[11] Metal foils coated with a carbon black paste show an improvement in thermal contact conductance, but the present work provides still higher values of the thermal contact conductance.

Solders have high thermal conductivity and are conformable in the molten state, but they suffer

Table XI. Comparison of thermal contact conductance for the solder–graphite composite and various materials from prior work tested with the same pressure and the same copper surfaces (the same composition and roughness)

Material	Thermal Contact Conductance [10^4 W/(m^2 K)] between Copper Surfaces of 15 μm Roughness		References
	0.46 MPa	0.92 MPa	
Type A solder–graphite	16.39 ± 0.21	26.22 ± 0.62	This work
Carbon–silver mixture paste	11.45 ± 0.82	14.35 ± 1.00	3
Graphite nanoplatelet paste	11.72 ± 0.28	12.36 ± 0.10	7
Carbon black (Tokai) paste	11.27 ± 0.34	13.18 ± 0.11	6
Silver paste (Arctic Silver 5)	9.79 ± 1.01	8.63 ± 0.37	3
Carbon black (Cabot) paste	8.73 ± 0.27	11.26 ± 0.36	5
Carbon black (Cabot) paste	8.45 ± 0.11	10.58 ± 0.11	10
Graphite flake paste	8.28 ± 0.51	8.46 ± 0.33	5
Ceramic particle paste (Ceramique)	7.21 ± 0.10	9.92 ± 0.41	3
Flexible graphite (50 μm) penetrated with Tokai carbon black paste	7.17 ± 0.23	–	50
Flexible graphite (50 μm) penetrated with Cabot carbon black paste	6.90 ± 0.21	–	50
Silver paste (Arctic Silver 3)	6.15 ± 0.65	6.22 ± 0.26	3
Flexible graphite (50 μm) coated with Cabot carbon black paste	4.78 ± 0.07	–	50
Flexible graphite (50 μm) coated with Tokai carbon black paste	4.67 ± 0.07	–	50
Aluminum foil (7 μm) coated with carbon black paste	3.67 ± 0.31	5.22 ± 0.45	2
Copper foil (13 μm) coated with carbon black paste	3.47 ± 0.17	3.95 ± 0.29	2
Boron nitride particle paste	2.89 ± 0.07	4.79 ± 0.19	5
Flexible graphite (130 μm) coated with carbon black paste	2.93 ± 0.09	3.28 ± 0.12	2
Flexible graphite (130 μm, uncoated)	1.40 ± 0.09	2.08 ± 0.11	2

The prior work is all by one of the authors (D.D.L.C.). The entries are listed in decreasing order of thermal contact conductance.

from their high CTE (which causes thermal fatigue) and the tendency for forming voids[52] (which decreases the thermal contact conductance[34]). At a thickness of 0.26 mm, the thermal contact conductance reported is up to 17.0×10^4 W/(m^2 K),[34] which is lower than the highest value obtained in this work.

A laminate of multiple flexible graphite sheets (50 μm to 200 μm thick per sheet) bonded together by soldering gives in-plane thermal contact conductance up to $(29 \pm 4) \times 10^4$ W/(m^2 K),[42,43] which is essentially equal to the highest value of $(26.2 \pm 0.6) \times 10^4$ W/(m^2 K) obtained in this work by using a solder–graphite network composite. Both the laminate of Refs. 42, 43 and the composites of this work require solder reflow during installation as a TIM. However, the composite fabrication process is more complicated for the laminate of Refs. 42, 43, since it involves electroplating of solder on flexible graphite[42] prior to lamination and cutting of the laminate in the through-thickness direction with subsequent lapping to form slices of thickness around 200 μm to 250 μm to serve as TIMs with the heat flow direction along the thickness of a slice.[43] The difficulty of fabricating TIMs of thickness below 200 μm is another drawback of this laminate route. Since the thermal resistance within the TIM decreases with decreasing thickness, small thicknesses are attractive.

The graphite–solder laminate of prior work[42,43] contains around 10 vol.% solder, whereas the solder–graphite composites of this work contain around 55 vol.% solder. Reference 42 mentions that the conformability of the TIM rather than the thermal conductivity of the TIM governs the TIM performance and that the conformability of the TIM stems from that of the graphite part of the laminate. At thickness below 110 μm, the solder–graphite composite of this work has its sandwich thermal resistance dominated by the composite–copper interfacial thermal resistance (Table VII), indicating that the conformability of the TIM rather than the thermal conductivity of the TIM governs the TIM performance. Hence, conformability is key for both the laminate of Refs. 42, 43 and the solder–graphite composite of this work. However, in contrast to the laminate, the conformability of the composite of this work is largely contributed by the solder, as indicated by the much higher interfacial thermal resistivity for the unmodified flexible graphite[50] compared with the solder–graphite composite of this work.

Tin nanowire arrays[53] show small dependence on the contact pressure, but the conformability is not adequate. A very high value of the thermal conductivity [67 W/(m K)] has been reported for tin nanowires, but the thermal contact conductance for tin nanowires [5.0×10^4 W/(m^2 K)] is less than that

of the present work [up to 26×10^4 W/(m^2 K)]. Similar research has been done on silver nanowire array composites.[54] A thermal conductivity of 38.8 W/(m K) (comparable to the value provided by the solder–graphite composite of this work) has been achieved, but the contact thermal conductance is only 2.0×10^4 W/(m^2 K).

Carbon nanotubes[12–20,55–57] and nanofibers[58] have received much recent attention in relation to their potential as TIMs. A thermal contact conductance of 1.6×10^4 W/(m^2 K) has been reported for a carbon nanotube adhesive grease.[57] A value of 5.6×10^4 W/(m^2 K) has been reported for carbon nanotube-filled silicone.[56] A value of 2×10^4 W/(m^2 K) has been reported for a mat comprising exfoliated graphite nanoplatelets, carbon nanotubes, and carbon nanofibers.[31] A value of 3.7×10^4 W/(m^2 K) has been reported for a carbon nanotube paper.[55] A value of 6.85×10^4 W/(m^2 K) has been reported for vertically aligned carbon nanotube arrays synthesized on a bulk aluminum alloy.[17] For a bilayer aligned carbon nanotube TIM,[16] the thermal contact conductance is up to 11.39×10^4 W/(m^2 K) and the thermal conductivity is up to 19.75 W/(m K). For a carbon nanotube array with an organic coating, a thermal contact conductance of 22×10^4 W/(m^2 K) has been reported.[15] For a carbon nanotube array that contains wax and is bonded to a surface by using a tin-based solder foil, a thermal contact conductance of 29×10^4 W/(m^2 K) has been reported.[14] For a carbon nanotube array that has been metallized with Ti/Au to facilitate bonding, a value of $(59 \pm 14) \times 10^4$ W/(m^2 K) has been reported for the array–substrate interface, which is an interface within the TIM.[13] The thermal resistance of an interface within a TIM is necessarily lower than that of the overall thermal contact between the two surfaces that sandwich the TIM. Therefore, the value of $(59 \pm 14) \times 10^4$ W/(m^2 K)[13] cannot be used for comparison of the performance of this TIM with that of other TIMs. For carbon nanofiber arrays,[58] the thermal contact conductance is up to 7.69×10^4 W/(m^2 K). Thus, all the reported values of thermal contact conductance (between the two surfaces that sandwich the TIM) for TIMs involving carbon nanotubes (CNTs) or carbon nanofibers (CNFs) are comparable to or lower than those for the solder–graphite composite of this work [up to 26×10^4 W/(m^2 K)]. This reflects the good conformability and high thermal conductivity of the solder–graphite composite of this work. Compared with the TIMs containing CNTs or CNFs, the composite of this work is advantageous in having much lower material cost. Compared with the TIMs in the form of CNTs or CNT arrays, the composite of this work is additionally advantageous in having much lower processing cost.

A lead-free-solder-matrix composite containing multiwalled carbon nanotubes has been reported.[36] Compared with the solder itself, a lower CTE value is obtained (19.3×10^{-6}/°C). However, the values obtained are high compared with those of the solder–graphite composites in this work.

CONCLUSIONS

A new low-cost high-performance TIM in the form of a solder–graphite composite sheet (≥55 vol.% solder) with a novel structure has been developed. In the composite, solder and graphite form interpenetrating networks to a degree. The material performs better than solder, flexible graphite, paste-coated flexible graphite, paste-penetrated flexible graphite, paste-coated metal foils, and a large variety of thermal pastes, all tested under identical conditions in the laboratory of one of the authors (D.D.L.C.). In addition, the material performs better than or is comparable to all previously reported TIMs that involve carbon nanotubes, carbon nanofibers or graphite/graphene nanoplatelets, which are more expensive than graphite.

The composite material is made by room-temperature compression of a mixture of ozone-treated exfoliated graphite and micrometer-size solder particles at 11.2 MPa to form the graphite network (due to the mechanical interlocking among the worms), followed by fluxless solder reflow (heating above the melting temperature of the solder) to form the solder network. The ozone treatment greatly improves the solder connectivity in the resulting composite.

With type B solder (95.5Sn-4Ag-0.5Cu), composite thickness of 40 μm, and contact pressure of 0.92 MPa, the composite exhibits CTE of 10×10^{-6}/°C, thermal contact conductance between copper surfaces (15 μm roughness) of 26×10^4 W/(m^2 K), through-thickness thermal conductivity of 52 W/(m K), and composite–copper interfacial thermal resistivity of 1.4×10^{-6} (m^2 K)/W, with about 75% of the thermal resistivity being due to the two composite–copper interfaces. This high performance requires the solder reflow (remelting the solder in the composite) while the composite is positioned at the thermal interface. No flux is required.

The composite is anisotropic, with the solder connectivity being much lower in the through-thickness direction than the in-plane direction and electrical conductivity anisotropy of 7.3. The electrical conductivity obeys the rule of mixtures (parallel model in-plane and series model through-thickness). The TIM performance is reduced slightly upon changing the solder from type B (95.5Sn-4Ag-0.5Cu) to type A (63Sn-37Pb), partly due to the higher thermal conductivity of type B solder.

The contact conductance exceeds or is comparable to that of all previously reported TIMs, provided that solder reflow has occurred and the composite thickness is ≤100 μm. Upon decreasing the thickness below 100 μm, the sandwich thermal resistivity decreases abruptly, the composite through-thickness thermal conductivity increases abruptly from 2 W/(m K) to 52 W/(m K) (reaching values comparable to

the values calculated based on the rule of mixtures for thermal resistors in parallel), and the composite–copper interfacial thermal resistivity (rather than the composite resistivity) becomes dominant. This means that the conformability rather than the thermal conductivity governs the TIM performance at thicknesses below 100 μm. Compared with the corresponding graphite without solder, the composite with thickness below 100 μm gives superior TIM performance, higher through-thickness thermal conductivity, and lower interfacial thermal resistivity (i.e., greater conformability). The solder contributes largely to the conformability and the thermal conductivity of the solder–graphite composite.

The TIM performance is progressively reduced by decreasing the contact pressure from 0.92 MPa to 0.46 MPa and to zero. This is due to an increase in the interfacial thermal resistivity, which is in turn due to a decrease in conformability.

REFERENCES

1. D.D.L. Chung, *Adv. Microelectron.* 33, 8 (2006).
2. T.A. Howe, C.K. Leong, and D.D.L. Chung, *J. Electron. Mater.* 35, 1628 (2006).
3. C.K. Leong and D.D.L. Chung, *Carbon* 42, 2323 (2004).
4. C.K. Leong and D.D.L. Chung, *Carbon* 41, 2459 (2003).
5. C.K. Leong, Y. Aoyagi, and D.D.L. Chung, *J. Electron. Mater.* 34, 1336 (2005).
6. C. Lin and D.D.L. Chung, *Carbon* 45, 2922 (2007).
7. C. Lin and D.D.L. Chung, *Carbon* 47, 295 (2009).
8. A. Yu, P. Ramesh, M.E. Itkis, E. Bekyarova, and R.C. Haddon, *J. Phys. Chem. C* 111, 7565 (2007).
9. Y. Xu, X. Luo, and D.D.L. Chung, *J. Electron. Packag.* 122, 128 (2000).
10. C. Lin and D.D.L. Chung, *J. Mater. Sci.* 42, 9245 (2007).
11. C.K. Leong, Y. Aoyagi, and D.D.L. Chung, *Carbon* 44, 435 (2006).
12. M. Rosshirt, D. Fabris, C. Cardenas, P. Wilhite, T. Tu, and C.Y. Yang, *Mater. Res. Soc. Symp. Proc.* 1158, F03 (2009).
13. R. Cross, B.A. Cola, T. Fisher, X. Xu, K. Gall, and S.A. Graham, *Nanotechnology* 21, 445705 (2010).
14. J.R. Wasniewski, D.H. Altman, S.L. Hodson, T.S. Fisher, A. Bulusu, S. Graham, and B.A. Cola, *J. Electron. Packag.* 134, 020901 (2012).
15. J.H. Taphouse, O.L. Smith, S.R. Marder, and B.A. Cola, *Adv. Funct. Mater.* 24, 465 (2014).
16. H. Wang, J.Y. Feng, X.J. Hu, and K.M. Ng, *Chem. Eng. Sci.* 65, 1101 (2010).
17. Z.L. Gao, K. Zhang, and M.M.F. Yuen, *Nanotechnology* 22, 1 (2011).
18. D. Fabris, M. Rosshirt, C. Cardenas, P. Wilhite, T. Yamada, and C.Y. Yang, *J. Electron. Packag.* 133, 1 (2011).
19. A. Hamdan, J. Cho, R. Johnson, J. Jiao, D. Bahr, R. Richards, and C. Richards, *Nanotechnology* 21, 1 (2010).
20. D.D.L. Chung, *Carbon* 50, 3342 (2012).
21. C. Lin and D.D.L. Chung, *J. Electron. Mater.* 37, 1698 (2008).
22. S.H. Anderson and D.D.L. Chung, *Carbon* 22, 253 (1984).
23. D.D.L. Chung, *J. Mater. Sci.* 22, 4190 (1987).
24. M. Inagaki, F. Kang, and M. Toyoda, *Chem. Phys. Carbon* 29, 1 (2004).
25. X.H. Wei, L. Liu, J.X. Zhang, J.L. Shi, and Q.G. Guo, *J. Mater. Sci.* 45, 2449 (2010).
26. A. Celzard, J.F. Mareche, and G. Furdin, *Prog. Mater. Sci.* 50, 93 (2005).
27. S.G. Ionov, V.V. Avdeev, S.V. Kuvshinnikov, and E.P. Pavlova, *Mol. Cryst. Liq. Cryst. Sci. Technol. A* 340, 349 (2000).
28. D.D.L. Chung, *J. Mater. Eng. Perform.* 9, 161 (2000).
29. E.E. Marotta and S.J. Mazzuca, *IEEE Trans. Compon. Packag. Manuf. Technol.* 28, 102 (2005).
30. H.F. Lu, W.S. Kuo, and T.H. Ko, *SAMPE Conf. Proc.* 51, 1 (2006).
31. R.J. Warzoha, D. Zhang, G. Feng, and A.S. Fleischer, *Carbon* 61, 441 (2013).
32. S. Ganguli, A.K. Roy, R. Wheeler, V. Varshney, F. Du, and L. Dai, *J. Mater. Res.* 28, 933 (2013).
33. I. Dutta, R. Raj, P. Kumar, T. Chen, C.M. Nagaraj, J. Liu, M. Renavikar, and V. Wakharkar, *J. Electron. Mater.* 38, 2735 (2008).
34. C.P. Chiu, J.G. Maveety, and Q.A. Tran, *Microelectron. Reliab.* 42, 93 (2002).
35. K.H. Prakash and T. Sritharan, *Acta Mater.* 49, 2481 (2001).
36. S.M.L. Nai, J. Wei, and M. Gupta, *Mater. Sci. Eng. A* 423, 166 (2006).
37. C.T. Ho and D.D.L. Chung, *J. Mater. Res.* 5, 1266 (1990).
38. P.M. Raj, P.R. Gangidi, N. Nataraj, N. Kumbhat, G.C. Jha, and R. Tummala, *IEEE Trans. Compon. Packag. Manuf. Technol.* 3, 989 (2013).
39. L. Yang, C. Du, J. Dai, N. Zhang, and Y. Jing, *J. Mater. Sci. Mater. Electron.* 24, 4180 (2013).
40. H. Huang, X. Wei, F. Liao, and L. Zhou, *J. Wuhan Univ. Technol. Mater. Sci. Ed.* 24, 206 (2009).
41. Y.D. Han, H.Y. Jing, S.M.L. Nai, L.Y. Xu, C.M. Tan, and J. Wei, *Intermetallics* 31, 72 (2012).
42. H. Chen, Y. Zhao, and C. Chen, *Front. Heat Mass Transf.* 4, 013004 (2013).
43. Y. Zhao, D. Strauss, T. Liao, Y.C. Chen, and C.L. Chen, in *Proceedings of the ASME/JSME 2011 8th Thermal Engineering Joint Conference, AJTEC2011-44169*, vol. 3 (2011), pp. 83–89.
44. T. Oku, *J. Nucl. Sci. Technol.* 32, 816 (1995).
45. P. Chen and D.D.L. Chung, *Carbon* 77, 538 (2014).
46. T. Siewert, S. Liu, D.R. Smith, and J.C. Madeni, *Database for Solder Properties with Emphasis on New Lead-Free Solders* (National Institute of Standards and Technology and Colorado School of Mines, 2002, Release 4.0).
47. P. Chen and D.D.L. Chung, *Carbon* 61, 305 (2013).
48. D.D.L. Chung, *Carbon* 68, 646 (2014).
49. X. Luo, R. Chugh, B.C. Biller, Y.M. Hoi, and D.D.L. Chung, *J. Electron. Mater.* 31, 535 (2002).
50. K. Hu and D.D.L. Chung, *Carbon* 49, 1075 (2011).
51. X. Fu, W. Lu, and D.D.L. Chung, *Carbon* 36, 1337 (1998).
52. X. Hu, L. Jiang, and K.E. Goodson, in *20th IEEE SEMI-THERM Symposium* (2004), pp. 98–103.
53. B. Feng, F. Faruque, P. Bao, A.T. Chien, and S. Kumar, *Appl. Phys. Lett.* 102, 093105-1-4 (2013).
54. J. Xu, A. Munari, E. Dalton, A. Mathewson, and K.M. Razeeb, *J. Appl. Phys.* 106, 4310 (2009).
55. H. Chen, M. Chen, J. Di, G. Xu, H. Li, and Q. Li, *J. Phys. Chem. C* 116, 3903 (2012).
56. H. Chen, H. Wei, M. Chen, F. Meng, H. Li, and Q. Li, *Appl. Surf. Sci.* 283, 525 (2013).
57. R.N. Das, E. Chenelly, E. Kopp, D. Alcoe, M.D. Poliks, and V.R. Markovich, in *IEEE Electronic Components and Technology Conference 2012; 62nd*, pp. 1442–1447.
58. Y. Zhang, Y. Xu, E. Suhir, C. Gu, and X. Liu, *J. Phys. D* 41, 1 (2008).